Automated sarcomere structure analysis for studying cardiotoxicity in human pluripotent stem cell-derived cardiomyocytes

Cao, L.; Schoenmaker, L.; Den, S.A. ten; Passier, R.; Schwach, V.; Verbeek, F.J.

Citation

Cao, L., Schoenmaker, L., Den, S. A. ten, Passier, R., Schwach, V., & Verbeek, F. J. (2022). Automated sarcomere structure analysis for studying cardiotoxicity in human pluripotent stem cell-derived cardiomyocytes. *Microscopy And Microanalysis*, *29*(1), 254-264. doi:10.1093/micmic/ozac016

Microscopy and Microanalysis, 2023, **29**, 254–264
https://doi.org/10.1093/micmic/ozac016
Advance access publication 21 December 2022
Original Article

Microscopy AND
Microanalysis

Automated Sarcomere Structure Analysis for Studying Cardiotoxicity in Human Pluripotent Stem Cell-Derived Cardiomyocytes

Lu Cao[1],*, Linde Schoenmaker[2], Simone A. Ten Den[3], Robert Passier[3],[4], Verena Schwach[3], and Fons J. Verbeek[1]

[1]*Imaging and Bioinformatics Group, Leiden Institute of Advanced Computer Science (LIACS), Leiden University, Leiden 2333 CA, The Netherlands*
[2]*Division of Drug Discovery and Safety, Leiden Academic Centre for Drug Research, Leiden University, Leiden 2333 CC, The Netherlands*
[3]*Applied Stem Cell Technologies, TechMed Centre, University of Twente, Enschede 7522 NB, The Netherlands*
[4]*Department of Anatomy and Embryology, Leiden University Medical Centre, Leiden 2300 RC, The Netherlands*

***Corresponding author:** Lu Cao, E-mail: l.cao@liacs.leidenuniv.nl

Abstract

Drug-induced cardiotoxicity is one of the main causes of heart failure (HF), a worldwide major and growing public health issue. Extensive research on cardiomyocytes has shown that two crucial features of the mechanisms involved in HF are the disruption of striated sarcomeric organization and myofibril deterioration. However, most studies that worked on extracting these sarcomere features have only focused on animal models rather than the more representative human pluripotent stem cells (hPSCs). Currently, there are limited established image analysis systems to specifically assess and quantify the sarcomeric organization of hPSC-derived cardiomyocytes (hPSC-CMs). Here, we report a fully automated and robust image analysis pipeline to detect z-lines and myofibrils from hPSC-CMs with a high-throughput live-imaging setup. Phenotype measurements were further quantified to evaluate the cardiotoxic effect of the anticancer drug Doxorubicin. Our findings show that this pipeline is able to capture z-lines and myofibrils. The pipeline filters out disrupted sarcomere structures and irrelevant noisy signals, which allows us to perform automated high-throughput imaging for accurate quantification of cardiomyocyte injury.

Key words: cardiotoxicity, high-throughput imaging, hPSC-derived cardiomyocytes, image analysis, live imaging, myofibril identification, sarcomere structure

Introduction

Heart failure (HF) is a major and growing public health problem worldwide, with high morbidity, mortality, and costs (Roger et al., 2012). A prime cause of HF is drug-induced cardiotoxicity and this is routinely evaluated during drug development and therapeutic applications (Sachinidis, 2020). Furthermore, the cardiotoxic side effect of anticancer treatments is one of the leading causes of mortality in cancer survivors (Schwach et al., 2020). However, investigations of the underlying mechanisms of HF caused by these drugs are hampered by the lack of predictive *in vitro* and *in vivo* models for human (Sachinidis, 2020).

Thus, there is an urgent need for human *in vitro* systems that can better predict drug-induced cardiotoxicity early in the drug development process (Cao et al., 2020).

In recent years, human pluripotent stem cells (hPSCs) are increasingly being used for disease modeling to elucidate pathological mechanisms of multifactorial and monogenic diseases at the cellular level (Doss & Sachinidis, 2019). In addition to this, hPSC-CMs are able to represent significant genetic variants of the population which is necessary for the detection of cardiotoxicity in the early drug development process, because toxic side effects do not show up in every patient (Fakunle & Loring, 2012; Rouhani et al., 2014; Tofoli et al., 2016).

Examining the effects of anticancer drugs, especially anthracyclines, in CMs *in vitro* has demonstrated several types of cardiac injury. One important mechanism of cardiomyocyte injury is characterized by the disruption of the striated organization of sarcomeres, the smallest contractile units of CMs' muscle fibers (Sawyer et al., 2010). In addition, cardiotoxicity is also manifested as myofibril deterioration (Burridge et al., 2016). Therefore, sarcomeric organization is a crucial feature indicating cardiotoxicity in CMs. Doxorubicin is a highly effective anticancer drug prescribed for the treatment of a variety of cancer types. However, the long-term clinical use of Doxorubicin is limited, because of its cumulative dose-dependent cardiotoxicity and HF (Singal & Iliskovic, 1998).

Analysis of sarcomeric organization requires accurately extracting z-lines and myofibrils from an image. Z-line is the segment separating and linking two neighboring sarcomeres. However, even for experienced researchers, it is a challenging task to manually trace these structures in different treatment conditions. Furthermore, this process is labor-intensive, low throughput and there is a high interobserver variability. Therefore, image analysis techniques have become a key tool to extract sarcomere features such as Z-lines (marking the borders of sarcomeres) from images. Khadangi et al. (2019), for example, used contrast stretching and a Sobel operator

Received: March 3, 2022. **Revised:** August 16, 2022. **Accepted:** September 26, 2022

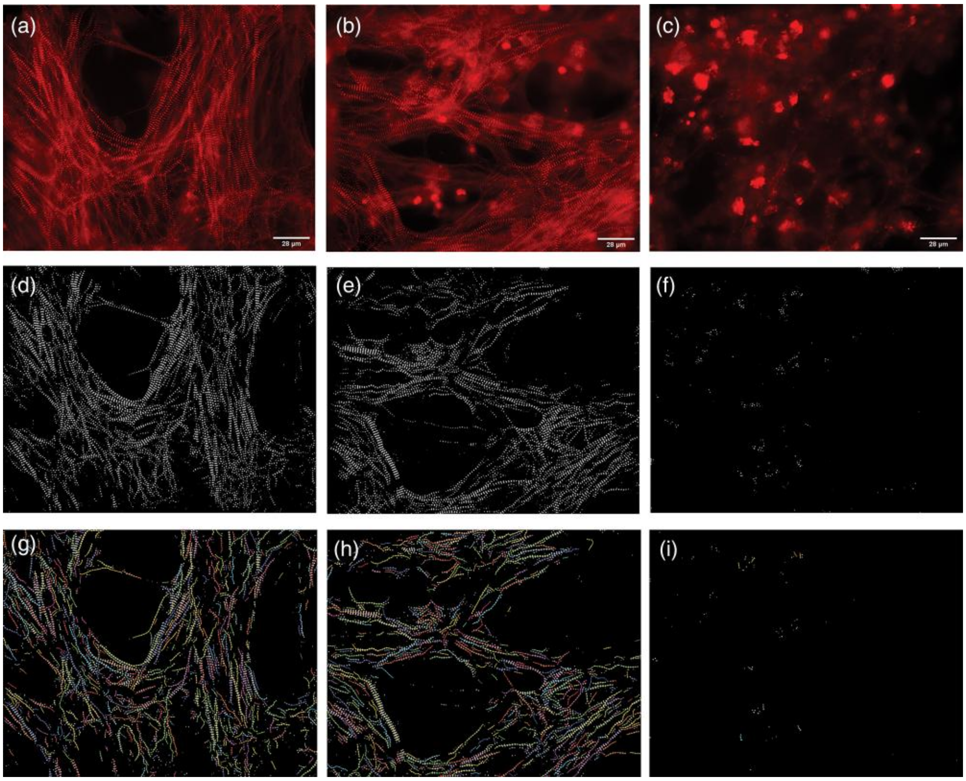

Fig. 1. Sample images acquired from EVOS live imaging microscope with a 40× objective. (**a**) Sample image in the control condition (DMSO). (**b**) Sample image with 1 μm Doxorubicin treatment on Day 1. (**c**) Sample image with 1 μm Doxorubicin treatment on Day 5. (**d–f**) Binary mask representing segmented z-lines from (**a–c**). (**g–i**) Result of myofibril tracing based on the binary mask (**d–f**). Contrast enhancement was applied to the sample images (**a–c**) using Enhance Contrast with Saturated pixels: 0.5% in ImageJ.

to segment Z-lines from serial block-face scanning electron microscopy images. To the same end, Morris et al. applied image analysis to segment sarcomere structures stained with alpha-Actinin, a protein localized at the z-lines, from fluorescent images. They first use a coherence anisotropic diffusion filter, contrast enhancement, and a top-hat filter for preprocessing. Subsequently, adaptive thresholding was used to segment the sarcomere structure stained with α-Actinin, a protein localized at the Z-lines, from fluorescent images. The α-Actinin skeleton and orientation were further extracted and cleaned so as to detect continuous z-lines in their application (Morris et al., 2020). Much less research has been performed on the automated identification of myofibrils; however, recently Varga et al. (2020) have shown that this is possible for highly ordered myofibrils. Most of the recently published work, however, is restricted to animal models, such as Sprague-Dawley rats.

In our cardiotoxicity study, we use a stable transgenic hPSC fluorescent reporter line that we have recently developed, which expresses a fusion protein of α-Actinin and fluorescent mRubyII in combination with expression of green fluorescent protein (GFP) at the genomic locus of the cardiac transcription factor NKX2.5 (Ribeiro et al., 2020). This α-Actinin/NKX2.5 double reporter line (DRRAGN) allows live imaging of sarcomeric organization specifically in CMs. Compared with adult CMs derived from animal models, hPSC-CMs are relatively immature. Consequently, the sarcomere structure in hPSC-CMs is not always well-organized, which increases the difficulty of sarcomere detection. This specialized cell line is used to study the cardiotoxic effects of the anticancer drugs, such as Doxorubicin.

Here, we report on a fully automated and robust image analysis pipeline, designed for analyzing drug-induced cardiotoxicity by detecting z-lines and myofibrils from hPSC-CM images with a high-throughput live-imaging setup as shown in Figure 1. Our validation study confirms that this pipeline is able to capture z-lines and myofibrils. Distracting signals can be filtered out such as disrupted sarcomere structures and Doxorubicin signals from the nucleus. In addition, the phenotype measurements derived from z-lines and myofibrils are capable of depicting cardiotoxicity in a wide range of severity levels.

Materials and Methods

Preparation of the Cells

Double Reporter mRubyII-ACTN2 and GFP-NKX2.5 (DRRAGN) hPSCs were differentiated to hPSC-CMs using growth factor-based differentiation as described previously (Ribeiro et al., 2020) for live imaging. Around Day 14 of differentiation, cells were dissociated using TrypLe (ThermoFisher) and were FACS (fluorescence-activated cell sorting) sorted for α-ActininmRybyII/w-NKX2.5eGFP/w using the SH800S Cell Sorter (Sony Biotechnology). Double positive CMs were seeded into CellCarrier-96 well special optics plates (PerkinElmer), coated with vitronectin (ThermoFisher) at a density of 50,000 cells per well. The hPSC-CMs were maintained in a humidified incubator at 37°C and 5% CO_2 and were refreshed with CM-TDI medium twice a week (Birket et al., 2015). 10–12 days after seeding the hPSC-CMs were treated with dimethylsulfoxide (DMSO 4.23 mM) as control or with 1 μm of the anticancer drug Doxorubicin for 5 days. Doxorubicin was only added on Day 0.

For immunofluorescent staining of alpha-Actinin, GM25256 human-induced pluripotent stem cells (hiPSCs) were differentiated to CMs using growth factor-based differentiation. CMs were seeded into CellCarrier-96 well special optics plates (PerkinElmer), coated with vitronectin (ThermoFisher) at a density of 50,000 cells per well. The hiPSC-CMs were maintained in a humidified incubator at 37°C and 5% CO_2 and were refreshed with CM-TDI medium three times a week (Birket et al., 2015). Fourteen days after seeding the hiPSC-CMs were treated with dimethylsulfoxide (DMSO 4.23 mM) as control or with 0.1 or 1 μm of the anticancer drug Doxorubicin. Doxorubicin was only added on Day 0 and, subsequently, cells were refreshed with CM-TDI medium. Cells were fixed on Day 5.

Adult mouse CMs were isolated from the wild-type (WT) model (Schuldt et al., 2021). Cells were seeded into a 24-well plate with glass bottom and fixated afterward.

Fixation and Staining

Cells were fixated in 4% paraformaldehyde (PFA) for 20 min and washed with phosphate-buffered saline (PBS) for three times.

An antibody against α-Actinin was used to identify sarcomeres. HiPSC-CMs and adult mouse CMs were stained for alpha-Actinin using mouse anti-human alpha-Actinin (A7811, Sigma-Aldrich) and goat anti-mouse Alexa Fluor™ 647 (A21235, Fisher Scientific).

Cells were permeabilized using 0.1% Triton X100 in PBS for 8 min. After washing cells in PBS for three times, cells were incubated with the primary antibody in PBS, 2% Fetal Bovine Serum (FBS), and 5% goat serum at 4°C overnight. After washing with PBS for three times, cells were incubated with the secondary antibody in PBS, 2% FBS, and 5% goat serum at room temperature for 1.5 h. Cells were washed with PBS again for three times before DAPI (4′,6-diamidino-2-phenylindole) staining.

Screening

Images of hPSC-CMs were acquired using the high-throughput automated EVOS FL Auto 2 (ThermoFisher) microscope equipped with a 40x Super-apochromat Olympus objective (NA 0.95) (ThermoFisher, AMEP4754). The red channel (α-Actinin) for live imaging was acquired using a 531/20 excitation filter with an exposure time of 0.16 s plus 1x gain and a 593/40 emission filter (ThermoFisher, AMEP4652). The whole monolayer cell culture was scanned by automatically acquiring 55 images per well every 24 h for 5 days. During the 5 days, cells were maintained at 37°C and 5% CO_2 on the EVOS FL Auto 2 with the EVOS Onstage incubator (ThermoFisher).

For CMs stained with α-Actinin, we used Cy5 auto-configured light cube with an exposure time of 0.018 s plus 1x gain to capture fluorescent α-Actinin signal. Each well in the 96-well plate was scanned automatically for 59 images. The adult mouse CMs were sparsely seeded in the 24-well plate. Therefore, we captured the images manually.

Z-line segmentation

The high-throughput live-imaging setup can generate hundreds of thousands of images per day. Therefore, the automatic image analysis pipeline needs to be efficient enough to analyze the large-scale volumes at a fast pace and to be robust enough to handle the variation of fluorescent signals. As shown in Figure 1, not all the red channel signals represent z-lines. Apart from α-Actinin-positive z-lines, we also observed out-of-focus blurry signals, in the control situation. Once treated with Doxorubicin, sarcomere disassembly begins, as can be seen by a loss in striations and an increase in a more diffuse, higher intensity fluorescence throughout the cytoplasm (Fan et al., 2015), as shown in Figure 1. In the cell nuclei of Figure 1b, an increasing signal of accumulated Doxorubicin could also be observed (Chaikomon et al., 2018), which was expected since it is known that Doxorubicin emits red fluorescence (Doxorubicin is also known as the “red devil” for its color and toxic effects). In order to specifically identify α-Actinin-positive z-lines, and distinguish it from blurry, diffuse, and higher intensity fluoresce signals, we performed various image analysis steps.

Unfortunately, traditional edge detection or adaptive thresholding methods are not able to address these problems. In this paper, we try to solve this challenging segmentation problem using a 2D-FFT operator with a customized bandpass filter (Heideman et al., 1985). It has been previously described that the sarcomere length of hPSC-CMs is around 1.6–1.8 μm, while the sarcomere length of more matured human adult CMs is about 2.2 μm (Karbassi et al., 2020; Knight et al., 2021; Tsan et al., 2021). The sarcomere length of our CMs is measured around $1.73 \pm 0.015\ \mu$m at full relaxation and $1.54 \pm 0.014\ \mu$m at maximum contraction (Ribeiro et al., 2020). This prior knowledge can be converted to the frequency domain, which enables us to define the upper and lower limit for a bandpass filter. In our application, we select 1.6 μm as the average sarcomere length with a 0.4 μm distance to the upper or lower bound. Therefore, we set the upper bound of the sarcomere length to 2 μm and the lower bound to 1.2 μm. The conversion from the spatial domain to the frequency domain is realized using equation (1) (Efford, 2000):

$$\text{Frequency} = \frac{N}{R * \text{SL}}, \tag{1}$$

where N is the closest power of two with respect to the max(*width*, *height*) of the image; R is the pixel-to-micrometer ratio; and SL is the sarcomere length in the spatial domain. In our case, as illustrated in Figure 2, the max(*width*, *height*) of the image is the image width with 1,328 pixels and the next closest power of two is 2,048 pixels. The pixel-to-micrometer ratio is 5.6 pixels/μm. Consequently, we set the upper bound/radius in the frequency domain to 300 pixels and the lower bound/radius to 180 pixels w.r.t. the origin. These boundaries are sufficient to resolve the required detail for the sarcomeres.

The whole pipeline of the automatic z-line segmentation is shown in Figure 3. First, two image preprocessing steps were performed; namely, background subtraction (ImageJ, Subtract Background, 50 for α-Actinin channel) and contrast enhancement (ImageJ, Enhance Contrast, Saturated pixels: 0.3% for α-Actinin channel), which reduces the influence of the background and, at the same time, improves the foreground signal; cf. Figure 3b. Since the signal in the original images of the control condition is relatively weak, enhancing the

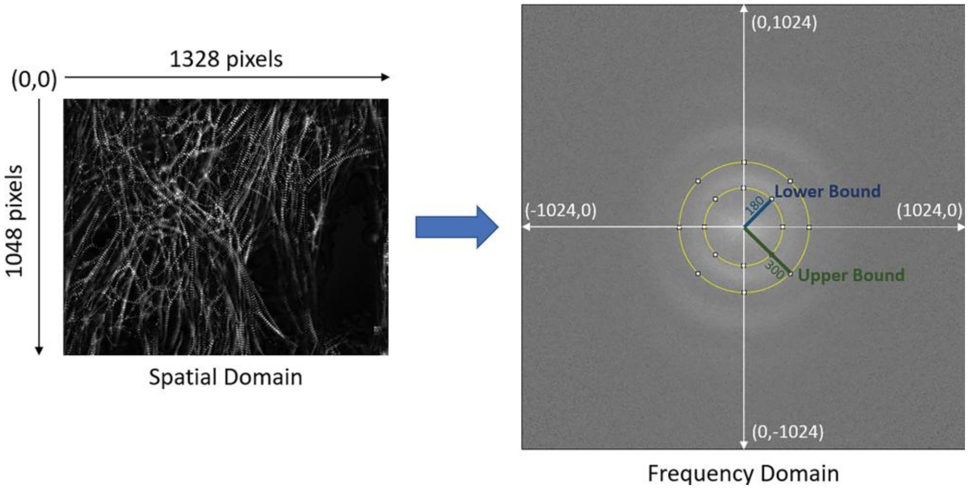

Fig. 2. Diagram of conversion from spatial domain to frequency domain.

contrast makes the intensity range better normalized and easier for thresholding. In addition, background subtraction removes low frequency signals such as out-of-focus blurriness and, in our case, enhances the details such as sarcomere structures. Preprocessing makes images more uniformly comparable. Second, a 2D-FFT is applied and a customized bandpass filter is used in the frequency domain to filter out low and high frequency signals so as to only include the range of frequencies that is representative to the range of sarcomere lengths (1.2–2 μm) as shown in Figures 3c and 3d. Subsequently, the bandpass filter is smoothed three times with a 3 × 3 percentile filter. Third, the inverse 2D-FFT is applied to retrieve the fluorescent signal that is in the predefined frequency range. Finally, an empirically derived threshold (threshold = 21 for 8-bit image) is used to filter out trivial signals and to acquire the binary mask representing the sarcomere structure as depicted in Figure 3f. Due to the variation of the conditions, hypotheses of adaptive thresholding methods are not always met which would make the results inconsistent. Therefore, a hard thresholding works better in our situation. The optimum threshold was derived by applying different thresholds to 100 images with varied conditions. After that, hard thresholding was considered representative. In this manner, we properly removed diffuse and higher intensity fluorescent signals and preserved the signals that represent z-lines. Even when the z-lines are largely disrupted as shown in Figure 1c, our method is still able to filter out highly expressed but irrelevant signals from the image.

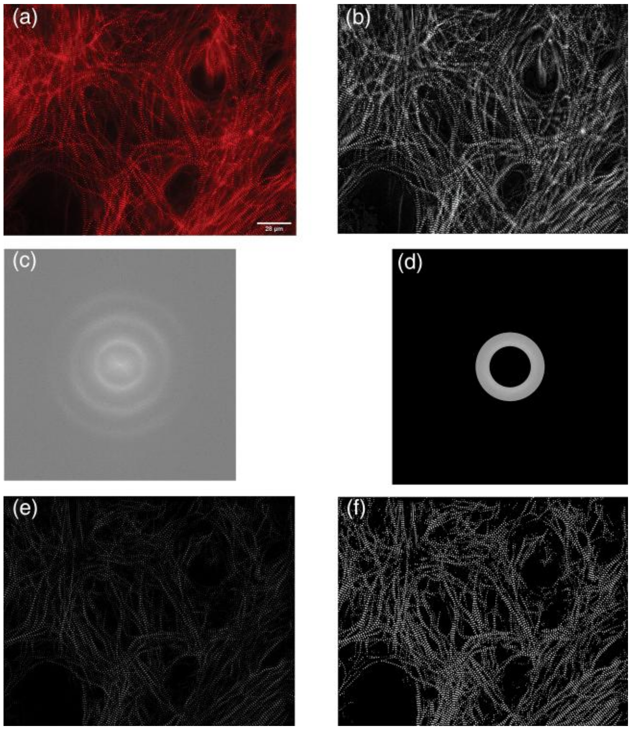

Fig. 3. Pipeline of automatic z-line segmentation. (**a**) Original image. (**b**) Result after preprocessing. (**c**) 2D-FFT result. (**d**) 2D-FFT with a customized bandpass filter. (**e**) Result of inverse 2D-FFT. (**f**) Binary mask after the thresholding.

Myofibril Identification

Another crucial characteristic of drug-induced cardiotoxicity is myofibril deterioration (Burridge et al., 2016). However, hPSC-CMs are known to display an immature myofibril alignment compared with native CMs (Sacchetto et al., 2020). In order to identify myofibrils from the images, a rule-based myofibril tracing method was designed (Fig. 4). Examples of myofibrils identified using this technique are shown in Figures 1g to 1i.

To link z-lines that are part of the same myofibril, a rule-based method was developed. Its flowchart is shown in Figure 4g. These rules are based on the following assumptions that are derived from general characteristics of sarcomeres and myofibrils.

1. Sarcomeres are demarcated by two z-lines at the lateral borders.
2. Sarcomeres have a narrow range of possible lengths (for our CMs between 1.2 and 2 μm), which translates to a minimum and maximum distance between two z-lines of a sarcomere.
3. Two z-lines that demarcate the lateral borders of the sarcomere are parallel to each other.
4. Myofibrils are relatively straight. It is unlikely for them to have sharp curves.

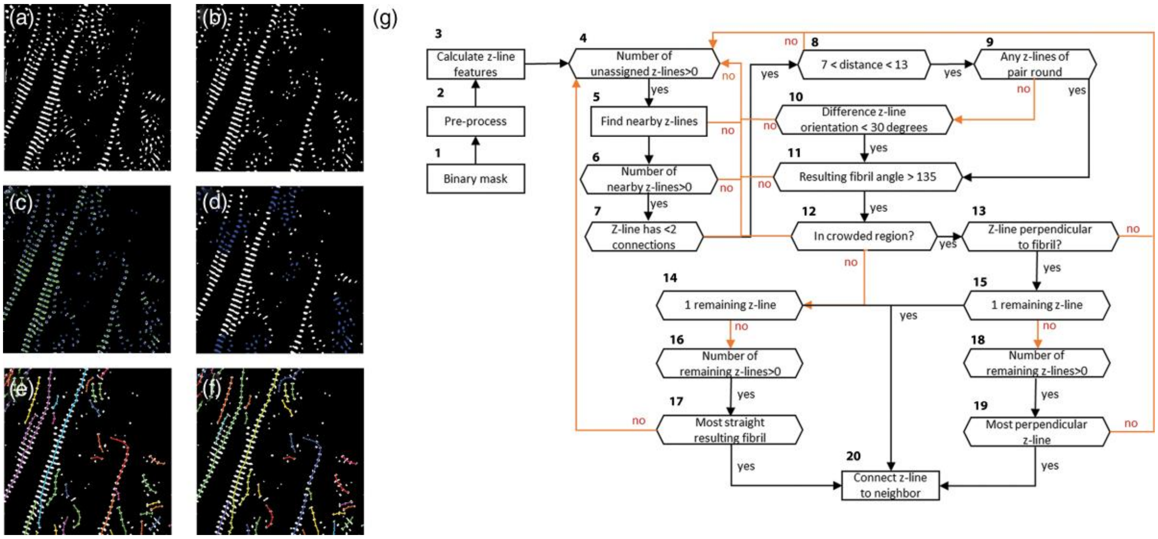

Fig. 4. Pipeline of automatic myofibril identification. (**a**) Cropped binary mask representing segmented sarcomere structure. (**b**) Result after preprocessing. (**c**) Object features; centroid and skeleton line. (**d**) Crowded regions. (**e**) Result of myofibril tracing. (**f**) Result after endpoint connection. Individual myofibrils are labeled. (**g**) Flowchart of the rule-based myofibril identification. All the parameters mentioned in the flowchart can be tuned.

5. z-lines are perpendicular to the length of the sarcomere and, therefore, perpendicular to the section of the myofibril that they are part of.

Before localizing the myofibrils, the binary z-line mask is preprocessed to disconnect overlapping z-lines as shown in Figures 4a and 4b, annotated as step 2 in Figure 4g. To this end, an opening operation is performed with a 3 × 3 cross-shaped structuring element. Subsequently, z-line features that are necessary for tracing are calculated at step 3 in Figure 4g. For all the objects in the preprocessed mask, the centroid coordinates are determined using the first moment integral of z-lines. Additionally, skeleton lines are generated and their orientations are derived from the slope of a least-squares line estimation (Zhang & Suen, 1984), as shown in Figure 4c. For round z-lines the orientation cannot accurately be estimated, instead these z-lines are assigned to the label "round" when their skeleton line is smaller than 0.71 μm, i.e., 4 pixels. This threshold was derived by applying different thresholds to a variety of z-lines and inspecting which threshold best distinguished between round and flat z-lines.

We observed that fibril tracing is more difficult in crowded regions, with multiple parallel myofibrils. Therefore, z-lines in crowded regions were identified at step 12 in Figure 4g by using a convolution operation with a uniform circular kernel (radius = 15.5 to represent 1.5 sarcomere length) on the binary centroid mask. The kernel will include three to four objects when it covers precisely one myofibril. To find the threshold that best describes crowded regions, successive thresholds were evaluated on images with varied conditions. Based on this, in regions where the sum of the object centroids in the kernel was higher than 7, the central element was assigned to the crowded region as shown in Figure 4d. Afterward, these regions are dilated with a circular structuring element (radius = 15.5) to include nearby z-lines.

For the rule-based connection method, the previously described criteria are evaluated for the identification of myofibrils. The first assumption follows that each z-line can be connected to a maximum of 2 other z-lines at step 7 in Figure 4g. The second rule for connection is that the Euclidean distance between the z-lines has to be between 1.25 and 2.32 μm, i.e., 7 and 13 pixels, respectively, at step 8 in Figure 4g. Based on the third assumption, the orientation of the z-lines is compared at step 10 in Figure 4g. A maximum difference of 30° was used as a threshold, because visual inspection of multiple angles showed that this resulted in the highest number of reasonable connections. The last criterion assesses the curve of the resulting fibril at step 11 in Figure 4g. Two z-lines are only connected if the angle between the two resulting sarcomeres is larger than 135°. To determine this threshold, multiple angels were evaluated and at angles below 135° the resulting myofibril was considered to be too curved. In cases where multiple suitable connections are found, the z-line that results in the straightest fibril is selected.

For z-lines in the crowded regions, an additional criterion is applied at step 13 in Figure 4g. The orientation of the fibril has to be roughly perpendicular to the z-line orientation. For this criterion, a range from 45° to 135° is used as the possible relative orientations. When multiple connections are found that fulfill all criteria, the sarcomeres that are the most perpendicular to the z-line orientation are chosen.

After applying these connection criteria to all the objects in the binary mask as shown in Figure 4e, an additional step is performed to connect any adjacent fibril endpoints. These endpoints are connected if the distance in between them is 2.5 μm, i.e., 14 pixels, or less and if the resulting fibril angles are larger than 120° and the sum of both angles is smaller than 360°. The final myofibril tracing result is shown in Figure 4f.

The myofibril tracing method was implemented in python using the image processing packages OpenCV and scikit-image (Gary, 2008; Van Der Walt et al., 2014). Moreover, a multiprocessing package was used to speed up the computing time.

Performance Evaluation

In order to evaluate the performance of the z-line segmentation, a quantitative assessment was conducted by comparing the results between the automated pipeline and the manual annotation. z-lines are highly dense signals in the image, especially in the control condition. Therefore, we cropped 10 images (256×256 pixels), with varied treatment conditions from the original image dataset. Two scientists with knowledge of our cardiotoxicity study were asked to independently segment the sarcomere structures from the images. Subsequently, we used the *F*-score (Du & Dua, 2010) to assess the accuracy of our segmentation method. The *F*-score is based on a calculation that takes into account both recall and precision. Recall (also known as sensitivity) is the proportion of real positive results that are correctly predicted positive. Precision (also known as specificity) denotes the proportion of predicted positive results that are real positives (Powers, 2011). The *F*-score is then calculated as follows:

$$F\text{-score} = 2\,\frac{\text{recall precision}}{\text{recall} + \text{precision}}. \tag{2}$$

We computed the *F*-score for our z-line segmentation method using the two manually segmented results. In addition, we compared the performance of our method to the zlineDetection method proposed by Morris et al. (2020). We used "Recommend Settings" to set the parameters in the software. The *F*-score of zlineDetection method is calculated based on the manual segmentation results as well.

In addition, we observed that variation exists between the sets of manual segmentation results. Because sarcomere structures are very small, researchers have different opinions on the size of the area that is covered by the α-Actinin signal. However, the annotated locations of sarcomere structures (z-lines) are consistent between the two researchers. Therefore, based on our observation and in order to overcome the variation between the manual segmentation results, we further applied a Union operator to combine the knowledge from the two manual annotations. The precision is calculated based on the following equation:

$$\text{Precision} = \frac{\text{TP}}{\text{Auto\_ROIs}}, \tag{3}$$

where TP is the number of true positive ROIs. In the binary mask derived from automatic segmentation, a labeled ROI is a true positive ROI as long as this ROI is fully or partially annotated in the binary mask from manual segmentation. Auto_ROIs is defined as the number of all the labeled ROIs in the binary mask from automatic segmentation.

The recall is calculated as follows:

$$\text{Recall} = \frac{\text{TP}}{\text{Manual\_ROIs}}, \tag{4}$$

where Manual_ROIs is defined as the number of all the labeled ROIs in the binary mask from manual segmentation. The same equations are applied to calculate the performance of the zlineDetection method developed by Morris et al. Only, instead of the segmentation result, the centerline is the final result of the zlineDetection method. Extra steps were taken to detect the local orientation of actinin and to eliminate off-target α-Actinin staining after segmentation to derive the final centerline. In order to fairly evaluate the performance of the zlineDetection method, we converted their final result: centerline as the binary mask to calculate the *F*1 score. In our performance measurement, only the location of all the z-lines is taken into account. Therefore, the *F*1 scores are comparable between our method and the zlineDetection method.

To evaluate the myofibril tracing algorithm the recall, precision, and *F*-score were calculated based on 36 cropped images (300×300 pixels) that we manually traced. The evaluation was performed on the sarcomere as well as the myofibril level. On the sarcomere level, a true positive is a sarcomere (described as a combination of two z-lines) that is present in the annotated version and the method's prediction. On the myofibril level, a true positive is an annotated fibril of which 50% or more is covered by one predicted fibril, similarly to the evaluation approach commonly used in cell tracking (Akram et al., 2016).

Results

Performance Evaluation

Performance Evaluation of Sarcomere Segmentation

To quantify the performance of the z-line segmentation methods, two researchers were asked to manually segment around 3075 ROIs representing z-lines from 10 randomly selected

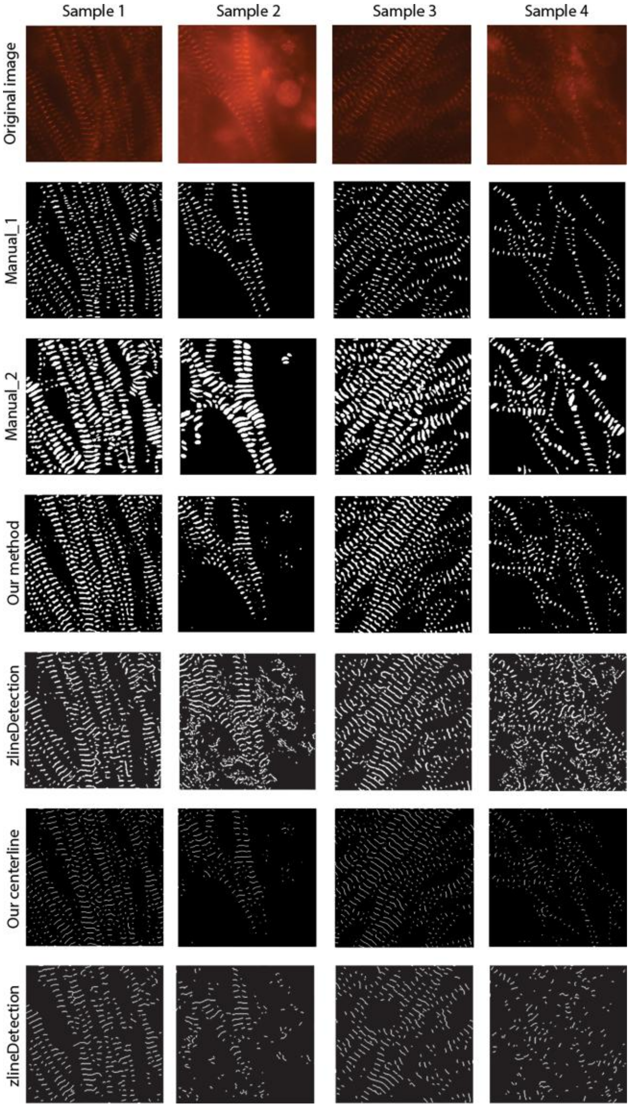

Fig. 5. Sample original images and results of manual segmentation, automated segmentation using our method and zlineDetection.

Table 1. *F*-score analysis for the automated and manual segmentation results.

		Manual_1			Manual_2			Manual_1 ∪ Manual_2		
	3,075 samples	Precision	Recall	*F*-Score	Precision	Recall	*F*-Score	Precision	Recall	*F*-Score
zlineDetection	Mean	**0.6291**	**0.5833**	**0.5360**	**0.5067**	**0.9500**	**0.6097**	**0.6439**	**0.6199**	**0.6151**
	SEM	0.0813	0.0752	0.0403	0.0810	0.0527	0.0660	0.0820	0.0386	0.0594
Our method	Mean	**0.7209**	**0.8000**	**0.7464**	**0.5753**	**1.0**	**0.7215**	**0.7389**	**0.8933**	**0.8018**
	SEM	0.0311	0.0861	0.0542	0.0454	0.0	0.0382	0.0323	0.0301	0.0209

Columns: Manual_1 and Manual_2 compare the manual segmentation to automated methods separately.
Columns: Manual_1 ∪ Manual_2 compares the union of the two manual segmentations to automated methods.
The bold values are the mean values of Precision, Recall and F-Score of the automated and manual segmentation methods.

images of our sample set with varied treatment conditions as shown in Figure 5. The automatic segmentation results, as well as the extracted centerlines from our method and the zlineDetection method, are shown in Figure 5. Researchers were able to accurately identify sarcomere structures when the cells are in the control condition (Fig. 5: Sample 1 and Sample 3). In contrast, it was more difficult for the researchers to precisely identify the ROIs in the treated condition (Fig. 5: Sample 2 and Sample 4) where the sarcomere structures were either disrupted or obscured by the increasingly accumulated Doxorubicin signal in the nucleus (Chaikomon et al., 2018). Due to the fact that Doxorubicin emits red fluorescence which is quite similar to the α-Actinin signal, identification of sarcomere structures is more challenging for both manual and automatic methods.

The results of the *F*-score analysis of all sarcomere segmentation methods are summarized in Table 1. When comparing the manual segmentation to automated methods separately, our method reaches a higher precision (72.09%, 57.53%), recall (80%, 100%), and *F*1 score (74.64%, 72.15%). A lower precision score in Manual_2 compared to Manual_1 is caused by the lower number of sarcomeres that were selected by the second researcher. In return, the recall score is much higher in Manual_2 compared with Manual_1. When using the union of the two sets of manual segmentations as a baseline, our method has a higher precision score (73.89%) and recall score (89.33%), than the zlineDetection method (64.39%, 61.99%, resp.). The relatively low precision and recall scores of the zlineDetection method are mainly caused by the α-Actinin signal of disrupted sarcomere structures and Doxorubicin signal in the nucleus, which obscures the α-Actinin signal of sarcomere structures from the image. Consequently, the *F*-score of our method (80.18%) is much higher than the zlineDetection method (61.51%). The higher performance of our method is caused by the customized band-pass filter which successfully filters out the α-Actinin signal of disrupted sarcomere structures and Doxorubicin signal in the nucleus. Our method is especially designed to apply on human CMs which uses large, high-resolution images as input (1,328 × 1,048 per image). Our method is able to segment the sarcomere structure per image in ∼1 s (PC with i7 processor and 8 GB RAM) which is especially suitable for a high-throughput setup.

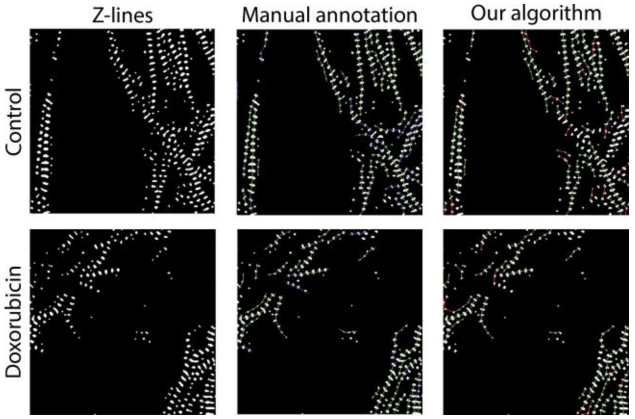

Fig. 6. Manual and automated myofibril tracing results. z-lines is the preprocessed binary mask on which the automated tracing was performed. The ground-truth myofibrils, including true positive and false negative myofibrils, are labeled based on the identification by the automatic approach. For the automatic tracing, the true positive and false positive myofibrils are shown.

Performance Evaluation of Myofibril Identification

To evaluate the myofibril tracing approach, the performance was analyzed qualitatively and quantitatively. For the qualitative evaluation, the results of the manual and automated tracing are shown on representative example images from the control and Doxorubicin conditions in Figure 6. It is apparent from this figure that the majority of the myofibrils are correctly traced. Instances of incorrectly identified connections are shown in red. In some cases, these are myofibrils that are identified where there should not be any myofibrils. However, more often it is the case that myofibrils are extended in the wrong direction or are longer than they should be. Instances of myofibrils that are annotated but are missing in the automated result are shown in blue. It is very rare that whole myofibrils are not identified, but quite often the ends of myofibrils are not traced completely.

Because myofibrils are made up of individual sarcomeres, the tracing results were evaluated on the sarcomere level and the fibril level as shown in Table 2. Quantitative analysis of the tracing algorithm shows that the *F*-scores of the sarcomere and fibril evaluation are 77% and 76.5%, respectively. On the sarcomere level, the recall (79.94%) is higher than the precision (74.59%). On the fibril level, this difference is less pronounced. These results indicate that the rule-based

Table 2. *F*-score analysis of the automated and manual myofibril tracing results.

		Precision	Recall	*F*-score
Sarcomere	Mean	0.7459	0.7994	0.77
	SEM	0.0281	0.0289	0.0277
Fibril	Mean	0.7637	0.7724	0.765
	SEM	0.0308	0.0326	0.0304

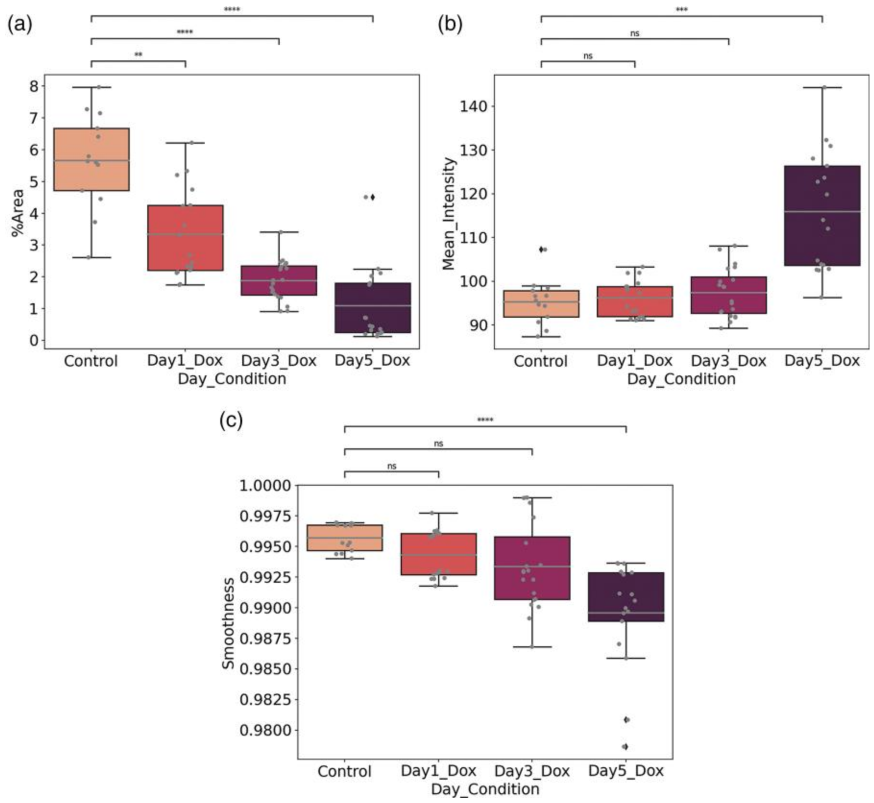

Fig. 7. Phenotypic measurement results of the z-lines of the control condition and on three separate days of 1 μm Doxorubicin treatment. (**a**) Results of the area fraction (%Area). (**b**) Results of the mean signal intensity. (**c**) Results of the smoothness. Mann and Whitney *U*-test was performed. *p*-value annotation legend: $**1.00\times10^{-03} < p <= 1.00\times10^{-02}$; $***1.00\times10^{-04} < p <= 1.00\times10^{-03}$; $****p <= 1.00\times10^{-04}$.

method gives reasonable results compared with manual tracing.

Case Study of Doxorubicin Exposure through Time

In order to show the ability of our image analysis pipeline to detect cardiotoxic effects, we collected and compared images of hPSC-CMs from the control condition (DMSO) and of Day 1, Day 3, and Day 5 of Doxorubicin exposure. In total, 2,134 images were collected for the three experimental replicates. Two sample images are shown in Figures 1a and 1c. We observed that, compared with the control condition, the treated condition shows big differences in terms of the area covered with z-lines and the average signal intensity in the region of interest (ROI). Therefore, after segmentation, we quantified the area fraction (%Area), mean intensity (Mean of the Signal Intensity), and texture as expressed by the smoothness. Smoothness describes the variance of intensity in the ROI (Gonzalez & Woods, 2018). We use it to differentiate homogeneous sarcomere texture in the control condition and diffuse texture in the treated condition. We averaged the measurements of all pictures in a well for comparison as shown in Figure 7. The area fraction stands for the percentage of pixels detected as z-lines in the original image. The mean signal intensity value is the average intensity value within the ROIs. The texture parameter smoothness is calculated as follows:

$$\text{Smoothness} = 1 - \frac{1}{(1+\sigma^2)}, \tag{5}$$

where σ is the standard deviation of the intensity values within the ROIs.

As we can see from Figure 7, the area fraction of z-lines is drastically reduced on Day 1 (3.33%) compared with the control condition (5.65%). The decreasing trend lasts till Day 5 (1.08%). The mean signal intensity slightly increases on Days 1 and 3, with 96.24 and 97.40, respectively, but significantly increases on Day 5 (115.93) compared with the control condition (95.30). In addition, the smoothness is also significantly reduced on Day 5 (0.9896) compared with the control condition (0.9957). This indicates that Doxorubicin treatment leads to a higher variation in intensity value in the ROIs. The increased signal in the cytoplasm, as shown by the mean intensity value and the smoothness, is another indication of sarcomere disassembly. These results demonstrate that the disruption of z-lines starts on Day 1 and is strongly manifested on Day 5.

In order to describe the impact of Doxorubicin on myofibrils, for each image the number of myofibrils, the average myofibril length and width, the percentage of assigned z-lines, and the randomness of the myofibril orientations were measured. The myofibril length was derived from the myofibril line going through all the successive centroids of z-lines. The length of this line was calculated using function arclength in OpenCV library (Gary, 2008) and converted to μm. To approximate the myofibril width, the maxima in the distance map derived from the binary mask (distance of z-line pixels to the line representing the myofibril) multiplied by two was used. The percentage of assigned z-lines is the number of z-lines that are part of myofibrils divided by the total number of z-lines in the segmented mask. To describe the uniformity of

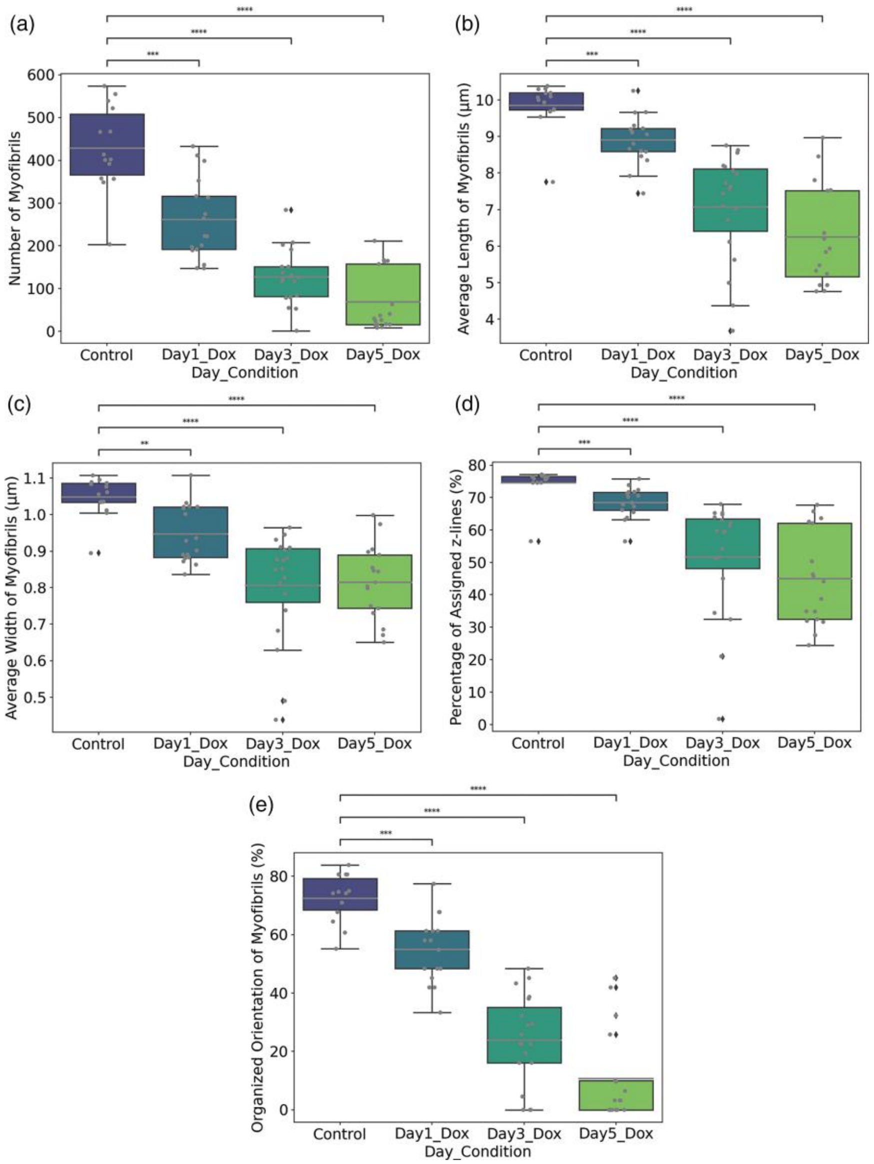

Fig. 8. Phenotypic measurement results of myofibrils from the control condition and on three separate days of 1 μm Doxorubicin treatment. (**a**) Number of myofibrils. (**b**) Average myofibril length. (**c**) Average myofibril width. (**d**) Percentage of assigned z-lines. (**e**) Percentage of images with organized orientation of myofibrils per well. Mann and Whitney *U*-test was performed. *p*-value annotation legend: $**1.00\times10^{-03} < p <= 1.00\times10^{-02}$; $***1.00\times10^{-04} < p <= 1.00\times10^{-03}$; $****p <= 1.00\times10^{-04}$.

the organization, the orientation of each myofibril was categorized into one of four directions: horizontal, vertical, diagonal right, and diagonal left. To decrease the potential bias caused by shorter fragments, the histogram of the orientations was normalized using the length of the myofibrils. The resulting weighted histogram was compared to a discrete uniform distribution, representing the case of a random distribution. The difference between the two distributions was quantified using the *p*-value from the chi-squared test. Lastly, we averaged the measurements of all pictures in a well for comparison. For the orientation of myofibrils, we counted the number of images in a well that have organized orientation. It is realized by counting images with the *p*-value smaller than 0.05.

As shown in Figure 8, the number of myofibrils is rapidly reduced; from 428 in the control condition to 261 in the treated condition on Day 1. It keeps reducing after Day 1 until it reaches 69 on Day 5. The average length of myofibrils reduces gradually through time: 9.85 μm in the control condition, 8.91 μm on Day 1, 7.07 μm on Day 3, and 6.25 μm on Day 5. An abrupt decrease is observed in the average width of myofibrils on Day 1 which is 0.95 μm compared with 1.05 μm in the control condition. After Day 1, the width continues decreasing, with an average width of 0.81 μm on Day 3 and 0.82 μm on Day 5. The percentage of assigned z-lines also decreases over time. It is 74.52% in control condition, 68.49% on Day 1, 51.78% on Day 3, and 44.99% on Day 5. It indicates that z-line organization decreases. The orientation of myofibrils is highly disrupted on Day 3 and Day 5 (23.90% and 10.65%, respectively) compared with the control condition where the percentage equals 72.42%. These results indicate a clear structural effect of Doxorubicin exposure over time.

An additional case study is provided in Supplementary material to investigate the generalization of our pipeline by testing on a widely accepted traditional method with α-Actinin-stained sarcomeres.

Discussion and Conclusion

In this paper, we describe a fully automated image analysis pipeline, that is able to reliably identify z-lines and myofibrils even with interference from other signals. By applying a 2D-FFT with a customized bandpass filter, we are able to detect/classify sarcomere structures from varied conditions of immature hPSC-CMs and even adult mouse CMs. In addition, the rule-based myofibril identification method shows the capacity of finding myofibrils. A clear effect of Doxorubicin exposure is shown using these methods. It drastically reduced the computation time (~1 s per image) which is particularly suitable in processing image datasets captured from high-throughput imaging setups.

According to performance evaluations, our method demonstrates a superior capability of handling wide-ranging fluorescent signals between experiments and is able to capture z-lines and myofibrils for studying cardiotoxicity. We have been able to quantify multiple phenotype measurements describing z-lines and myofibrils, which clearly indicate disruption of sarcomere structures in the cardiotoxicity study. The present study raises the possibility that evaluations of the quality of striated CMs can be performed by our phenotype analysis. Similarly, to manual extraction of sarcomeric z-lines from images and providing metrics that encapsulate different aspects of the z-line architecture, our method is able to quantify morphology, texture, and orientation features of sarcomere structures.

Our image analysis pipeline enables automated testing the cardiotoxicity of drugs which is required for all drugs before entering clinical trials and ultimately the market. Moreover, hPSC-based assays are recommended by the Food and Drug Administration (FDA) for performing these tests (Colatsky et al., 2016). Our method has shown to be particularly efficient in the processing of large images of hPSC-CMs and can be combined with our previous findings on evaluating cardiotoxicity based on phenotypic changes in hPSC-CMs (Cao et al., 2020). High-throughput analysis of phenotypical readouts can be combined with other high-throughput assays using functional and biochemical parameters, such as cardiomyocyte contractility, electrophysiology, calcium signaling, and mitochondrial activity (van Meer et al., 2016), which together will provide detailed information on drug responses and clinically relevant cardiac disease phenotypes *in vitro*. Moreover, the use of hPSC-CMs facilitates studying patient-to-patient variations, which is of utmost importance for patient stratification, repurposing of drugs. In addition, this image analysis pipeline can further facilitate the progress of personalized medicine by helping to predict for which patients' therapies will be safe (Schwach et al., 2020). In summary, our image analysis pipeline provides a fully automated and accurate method for the evaluation of the sarcomere structure during drug-induced cardiotoxicity in hPSC-CMs and is a valuable tool for studying cardiac disease *in vitro*.

For future work, we intend to verity the translatability of our analysis platform to a "real-world" scenario (i.e., cardiomyocytes). We have shown the possibility of using our sarcomere detection method to analyze adult mouse CMs. In the future, we will adjust our analysis platform to analyze primary CMs. For example, our finding of changes in the first day of Doxorubicin exposure in hPSC-CMs can be readily translated to rodent primary CMs, which have been previously cultured in a short time frame. Our follow-up step is to explore deep learning models, especially Deep Convolutional Neural Networks (DCNNs) for object detection such as U-Net (Ronneberger et al., 2015), Mask-RCNN (He et al., 2018), and YOLOv4 (Bochkovskiy et al., 2020). These are popular methods for object detection with a fast-processing speed (≤1 s per image) and are therefore well suited for a high-throughput setup. We intend to evaluate the performance of these models for the segmentation of the z-lines and its further improvement in myofibril identification. A limitation of our tracing approach is that the connections of each z-disk are only considered once. Finding the most optimal connections by exploring the application of deep learning techniques could therefore further improve the myofibril identification. Our validated automated segmentation method can be used to automatically annotate the training data, after further curation steps are considered. In addition, sarcomere and myofibril disruption in 3D space will be further explored and included in our existing pipeline. In the future, we hope we can include deep learning models in our standardized pipeline to analyze sarcomere and myofibril both in 2D and 3D spaces. Our pipeline will be applied to evaluate the cardiotoxicity effect of other drugs. Moreover, our research will assess distributed computing so as to balance the computational load between graphics processing unit (GPU) and central processing unit (CPU).

Supplementary material

To view supplementary material for this article, please visit https://doi.org/10.1093/micmic/ozac016.

Acknowledgments

We thank Dr. Diederik Kuster in Amsterdam UMC for providing adult mouse cardiomyocytes for testing. This work was supported by ERA-CVD 2016T092 and the Dutch Heart Foundation.

Conflict of interest

The author(s) declare none.

References

Akram SU, Kannala J, Eklund L, & Heikkila J (2016). Cell proposal network for microscopy image analysis. Proceedings of the International Conference on Image Processing (ICIP), August 19, 2016, pp. 3199–3203. Phoenix, AZ: IEEE.

Birket MJ, Ribeiro MC, Kosmidis G, Ward D, Leitoguinho AR, van de Pol V, Dambrot C, Devalla HD, Davis RP, Mastroberardino PG, Atsma DE, Passier R & Mummery CL (2015). Contractile defect caused by mutation in MYBPC3 revealed under conditions optimized for human PSC-cardiomyocyte function. *Cell Rep* **13**(4), 733–745.

Bochkovskiy A, Wang CY & Liao HYM (2020). YOLOv4: optimal speed and accuracy of object detection. *arXiv*:2004.10934.

Burridge PW, Li YF, Matsa E, Wu H, Ong SG, Sharma A, Holmström A, Chang AC, Coronado MJ, Ebert AD, Knowles JW, Telli ML, Witteles RM, Blau HM, Bernstein D, Altman RB & Wu JC (2016). Human induced pluripotent stem cell-derived cardiomyocytes recapitulate the predilection of breast cancer patients to Doxorubicin-induced cardiotoxicity. *Nat Med* **22**(5), 547–556.

Cao L, der Meer ADV, Verbeek FJ, & Passier R (2020). Automated image analysis system for studying cardiotoxicity in human pluripotent stem cell-derived cardiomyocytes. *BMC Bioinformatics*, **21**(1), 187.

Chaikomon K, Chattong S, Chaiya T, Tiwawech D, Sritana-Anant Y, Sereemaspun A & Manotham K (2018). Doxorubicin-conjugated dexamethasone induced MCF-7 apoptosis without entering the nucleus and able to overcome MDR-1-induced resistance. *Drug Des Devel Ther* **12**, 2361–2369.

Colatsky T, Fermini B, Gintant G, Pierson JB, Sager P, Sekino Y, Strauss DG & Stockbridge N (2016). The Comprehensive in vitro Proarrhythmia Assay (CiPA) initiative—Update on progress. *J Pharmacol Toxicol Methods* **81**, 15–20.

Doss MX & Sachinidis A (2019). Current challenges of iPSC-based disease modeling and therapeutic implications. *Cells* **8**(5). 403.

Du X & Dua S (2010). Segmentation of fluorescence microscopy cell images using unsupervised mining. *Open Med Inform J* **4**(1), 41–49.

Efford N (2000). *Digital Image Processing: A Practical Introduction Using Java*. Boston: Addison-Wesley.

Fakunle ES & Loring JF (2012). Ethnically diverse pluripotent stem cells for drug development. *Trends Mol Med* **18**(12), 709–716.

Fan X, Hughes BG, Ali MAM, Cho WJ, Lopez W & Schulz R (2015). Dynamic alterations to α-actinin accompanying sarcomere disassembly and reassembly during cardiomyocyte mitosis. *PLoS ONE* **10**(6). e0129176.

Gary B (2008). The openCV library. *Dr. Dobb's J Softw Tools* **25**-(2236121), 120–123.

Gonzalez RC & Woods RE (2018). *Digital Image Processing*. Available at https://public.ebookcentral.proquest.com/choice/publicfullrecord.aspx?p=5573669

He K, Gkioxari G, Dollár P & Girshick R (2018). Mask R-CNN. *IEEE Trans Pattern Anal Mach Intell* **42**(2), 386–397.

Heideman MT, Johnson DH & Burrus CS (1985). Gauss and the history of the fast Fourier transform. *Arch Hist Exact Sci* **34**(3), 265–277.

Karbassi E, Fenix A, Marchiano S, Muraoka N, Yang X & Murry CE (2020). Implications for regenerative medicine. *Nat Rev Cardiol* **17**(6), 341–359.

Khadangi A, Hanssen E & Rajagopal V (2019). Automated segmentation of cardiomyocyte Z-disks from high-throughput scanning electron microscopy data. *BMC Med Inform Decis Mak* **19**(6), 272.

Knight WE, Cao Y, Lin YH, Chi C, Bai B, Sparagna GC, Zhao Y, Du Y, Londono P, Reisz JA, Brown BC, Taylor MRG, Ambardekar AV, Cleveland JC, McKinsey TA, Jeong MY, Walker LA, Woulfe KC, D'Alessandro A & Song K (2021). Maturation of pluripotent stem cell-derived cardiomyocytes enables modeling of human hypertrophic cardiomyopathy. *Stem Cell Reports* **16**(3), 519–533.

Morris TA, Naik J, Fibben KS, Kong X, Kiyono T, Yokomori K & Grosberg A (2020). Striated myocyte structural integrity: Automated analysis of sarcomeric z-discs. *PLoS Comput Biol* **16**(3), e1007676.

Powers DMW (2011). Evaluation: From precision, recall and F-measure to roc, informedness, markedness & correlation. *J Mach Learn Technol* **2**(1), 37–63.

Ribeiro MC, Slaats RH, Schwach V, Rivera-Arbelaez JM, Tertoolen LGJ, van Meer BJ, Molenaar R, Mummery CL, Claessens MMAE & Passier R (2020). A cardiomyocyte show of force: A fluorescent alpha-actinin reporter line sheds light on human cardiomyocyte contractility versus substrate stiffness. *J Mol Cell Cardiol* **141**, 54–64.

Roger VL, Go AS, Lloyd-Jones DM, Benjamin EJ, Berry JD, Borden WB, Bravata DM, Dai S, Ford ES, Fox CS, Fullerton HJ, Gillespie C, Hailpern SM, Heit JA, Howard VJ, Kissela BM, Kittner SJ, Lackland DT, Lichtman JH, Lisabeth LD, Makuc DM, Marcus GM, Marelli A, Matchar DB, Moy CS, Mozaffarian D, Mussolino ME, Nichol G, Paynter NP, Soliman EZ, Sorlie PD, Sotoodehnia N, Turan TN., Virani SS., Wong ND., Woo D, Turner MB & American Heart Association Statistics Committee and Stroke Statistics Subcommittee (2012). Heart disease and stroke statistics–2012 update: A report from the American Heart Association. *Circulation* **125**(1), e2–e220.

Ronneberger O, Fischer P, & Brox T (2015). U-Net: Convolutional networks for biomedical image segmentation. *Lect Notes Comput Sci (Including Subseries Lecture Notes in Artificial Intelligence and Lecture Notes in Bioinformatics)*, **9351**, 234–241.

Rouhani F, Kumasaka N, de Brito MC, Bradley A, Vallier L & Gaffney D (2014). Genetic background drives transcriptional variation in human induced pluripotent stem cells. *PLoS Genetics* **10**(6), e1004432.

Sacchetto C, Vitiello L, de Windt LJ, Rampazzo A & Calore M (2020). Modeling cardiovascular diseases with hiPSC-derived cardiomyocytes in 2D and 3D cultures. *Int J Mol Sci* **21**(9), 3404.

Sachinidis A (2020). Cardiotoxicity and heart failure: Lessons from human-induced pluripotent stem cell-derived cardiomyocytes and anticancer drugs. *Cells* **9**(4), 1001.

Sawyer DB, Peng X, Chen B, Pentassuglia L & Lim CC (2010). Mechanisms of anthracycline cardiac injury: Can we identify strategies for cardioprotection? *Prog Cardiovasc Dis* **53**(2), 105–113.

Schuldt M, Pei J, Harakalova M, Dorsch LM, Schlossarek S, Mokry M, Knol JC, Pham TV, Schelfhorst T, Piersma SR, Dos Remedios C, Dalinghaus M, Michels M, Asselbergs FW, Moutin MJ, Carrier L, Jimenez CR, Van Der Velden J & Kuster DWD (2021). Proteomic and functional studies reveal detyrosinated tubulin as treatment target in sarcomere mutation-induced hypertrophic cardiomyopathy. *Circ Heart Fail* **14**(1), e007022.

Schwach V, Slaats RH & Passier R (2020). Human pluripotent stem cell-derived cardiomyocytes for assessment of anticancer drug-induced cardiotoxicity. *Front Cardiovasc Med* **7**, 50.

Singal PK & Iliskovic N (1998). Doxorubicin-induced cardiomyopathy. *N Engl J Med* **339**(13), 900–905.

Tofoli FA, Dasso M, Morato-Marques M, Nunes K, Pereira LA, da Silva GS, Fonseca SAS, Costas RM, Santos HC, da Costa Pereira A, Lotufo PA, Bensenor IM, Meyer D & Pereira LV (2016). Increasing the genetic admixture of available lines of human pluripotent stem cells. *Sci Rep* **6**(1), 34699.

Tsan Y-C, DePalma SJ, Zhao Y-T, Capilnasiu A, Wu Y-W, Elder B, Panse I, Ufford K, Matera DL, Friedline S, O'Leary TS, Wubshet N, Ho KKY, Previs MJ, Nordsletten D, Isom LL, Baker BM, Liu AP & Helms AS (2021). Physiologic biomechanics enhance reproducible contractile development in a stem cell derived cardiac muscle platform. *Nat Commun* **12**(1), 1–16.

Van Der Walt S, Schönberger JL, Nunez-Iglesias J, Boulogne F, Warner JD, Yager N, Gouillart E & Yu T (2014). Scikit-image: Image processing in python. *PeerJ* **2**(1), e453.

van Meer BJ, Tertoolen LGJ & Mummery CL (2016). Concise review: Measuring physiological responses of human pluripotent stem cell derived cardiomyocytes to drugs and disease. *Stem Cells* **34**(8), 2008–2015.

Varga B, Meli AC, Radoslavova S, Panel M, Lacampagne A, Gergely C, Cazorla O & Cloitre T (2020). Internal structure and remodeling in dystrophin-deficient cardiomyocytes using second harmonic generation. *Nanomedicine* **30**, 102295.

Zhang TY & Suen CY (1984). A fast parallel algorithm for thinning digital patterns. *Commun ACM* **27**(3), 236–239.